Molecularly soldered covalent organic frameworks for ultrafast precision sieving

MATERIALS SCIENCE

Molecularly soldered covalent organic frameworks for ultrafast precision sieving

Yanqiu Zhang[1,2], Jing Guo[1], Gang Han[3], Yongping Bai[1], Qingchun Ge[4], Jun Ma[2], Cher Hon Lau[5], Lu Shao[1]*

The weak interlamellar interaction of covalent organic framework (COF) nanocrystals inhibit the construction of highly efficient ion/molecular sieving membranes owing to the inferior contaminant selectivity induced by defects in stacked COF membranes and stability issues. Here, a facile in situ molecularly soldered strategy was developed to fabricate defect-free ultrathin COF membranes with precise sieving abilities using the typical chemical environment for COF condensation polymerization and dopamine self-polymerization. The experimental data and density functional theory simulations proved that the reactive oxygen species generated during dopamine polymerization catalyze the nucleophilic reactions of the COF, thus facilitating the counter-diffusion growth of thin COF layers. Notably, dopamine can eliminate the defects in the stacked COF by soldering the COF crystals, fortifying the mechanical properties of the ultrathin COF membranes. The COF membranes exhibited ultrafast precision sieving for molecular separation and ion removal in both aqueous and organic solvents, which surpasses that of state-of-the-art membranes.

INTRODUCTION

With the rapid growth of the global economy and population, water scarcity has become an ineluctable threat to the survival and development of human society. It is projected that 4 billion to 5 billion people will suffer from global water shortage and water-borne illnesses by 2050 (*1*). One of the best examples is the COVID-19 pandemic, wherein the contamination of freshwater and sewage with the virus could pose potential health risks (*2*). Notably, one target of the Sustainable Development Goals (2015–2030) is to provide "clean, accessible water for all," which requires innovative technologies and materials that produce fit-for-purpose water from alternative water resources such as wastewater, seawater, and briny water (*3*). Membrane-based separations, featured by their high energy efficiency, superior performance, and highly selective transport of target chemicals (e.g., molecules and ions), have been considered as an ideal purification technology for industrial and domestic applications (*4*). However, most polymer membranes have a dense and amorphous structure; thus, an ineradicable "trade-off" relationship is observed between permeance and selectivity (*5*, *6*). Improving the membrane selectivity is often accompanied by a decrease in its permeance (*7*).

Covalent organic frameworks (COFs) have been considered as attractive alternative materials for advanced separations because of their high porosity, well-organized channel structures, and adjustable pore size, which are expected to break the trade-off associated with the traditional polymeric membranes during the separation processes (*8*–*10*). To date, researchers have mainly focused on the fabrication of self-standing COF membranes, which require a sufficient thickness (i.e., usually hundreds of micrometers) to provide the desirable mechanical stability for practical separations (*11*, *12*). This requirement inevitably compromises the membrane permeance. Notable efforts have also been devoted to transforming COF nanocrystals into continuous and selective membranes on porous substrates to prepare COF thin-film composite membranes. However, this approach suffers from structural instability during the COF nanocrystal dispersion, and the preparation of the COF nanocrystals generally requires harsh conditions such as high temperatures and aggressive solvents (*13*). In addition, inadequate interfacial adhesion between the COF layer and the substrate severely decreases the mechanical strength and operational durability of the as-prepared membrane. Alternatively, the in situ intergrown method could avoid the formation of defects arising from the gaps between the separation layer and the substrate, forming robust COF composite membranes with stringent interface compatibility (*14*, *15*). Nevertheless, in light of the two-dimensional (2D) layered COF composite membranes, the preparation of a defect-free COF selective layer on an underlying substrate via an in situ growth method at room temperature using green solvents remains a tricky challenge because of the rigid membrane formation conditions. Another critical issue is the effective manipulation of the pore aperture size of the COF membrane at the subnanometer scale to enable the precise separation of small molecules. To date, only a few studies have reported the synthesis of 2D COF membranes for small molecule separations via interfacial polymerization (*16*) and polymer-assisted techniques (*4*, *17*). One of the main challenges is the inferior molecular sieving effects of the conventional COFs because their pore sizes (i.e., 0.8 to 4.7 nm) are larger than the kinetic diameters of most nanoscale molecules and ions such as Na^+ (0.72 nm), Cl^- (0.66 nm), and SO_4^{2-} (0.76 nm) (*18*). Although difficult, the precise adjustment of the subnanometer pore sizes of COFs has been achieved through monomer design or group modification. In addition, the weak π-π interactions among the COF nanocrystals would lead to the poor mechanical strength of fabricated COF membranes for significant malfunction in practice. Therefore, it is highly desirable to develop new approaches that can simultaneously accomplish specific adjustment of pore sizes for

[1]MIIT Key Laboratory of Critical Materials Technology for New Energy Conversion and Storage, State Key Laboratory of Urban Water Resource and Environment, and School of Chemistry and Chemical Engineering, Harbin Institute of Technology, Harbin 150001, China. [2]School of Environment, Harbin Institute of Technology, Harbin 150009, China. [3]Department of Chemical Engineering, Massachusetts Institute of Technology, Cambridge, MA 02139, USA. [4]College of Environment and Resources, Fuzhou University, No. 2 Xueyuan Road, Fujian 350116, China. [5]School of Engineering, The University of Edinburgh, King's Buildings, Mayfield Road, Edinburgh EH9 3JL, UK.
*Corresponding author. Email: shaolu@hit.edu.cn

effective sieving, excellent mechanical strength, superior separation performance, and improved durability of the COF membranes.

Here, we have developed a facile in situ molecularly soldered method to fabricate defect-free COF membranes, demonstrating precise molecular sieving effects using the typical chemical environment for dopamine (DA) polymerization and condensation polymerization of a Schiff base COF(TpPa) comprising 1,3,5-triformylphloroglucinol (Tp) and *p*-phenylenediamine (Pa) at room temperature. Mussel-inspired DA can self-polymerize in an alkaline solution and react with Pa (*19*). Reactive oxygen species (ROS) generated during the polymerization of DA could accelerate the nucleophilic reaction for COF formation (*20*). Meanwhile, DA can react with amino-based monomers through Schiff base reactions (*21*). Notably, the Schiff base COFs can be synthesized in screened water/ethanol (EtOH) solutions with a pH above 8 because of the inherent basicity of Pa. The similar self-assembly environments for both materials enable the in situ soldering of COFs through constantly generated polydopamine (pDA) "threads." Through this one-step approach, we could firmly affix a pDA-patched defect-free COF dense layer on a porous substrate surface using green solvents under ambient conditions. Moreover, the covalent interactions of DA with the COF and COF ligands reduced the separation size of the membrane and greatly enhanced the mechanical properties and stabilities of the membranes. The precise molecular and ion sieving properties of the newly developed 2D COF membranes were used for ultrafast energy-efficient desalination and organic solvent nanofiltration.

RESULTS

The synthesis protocol for the molecularly soldered of 2D COF composite membranes with polyimide (PI) porous substrates is shown in Fig. 1. In a typical synthesis, DA hydrochloride was first dissolved in a Pa aqueous solution for 10 min. The alkalinity (pH 9.1) of the Pa-based aqueous solution promoted the self-aggregation of DA until the addition of an ethanolic solution comprising the organic linker of Tp. Although the introduction of Tp organic linkers into the Pa/DA hydrochloride mixture decreased the pH to ~8.08, the oxidation polymerization of DA was still initiated. Meanwhile, ROS generated from the DA self-polymerization reaction promoted the formation of TpPa-COF. On the other hand, the Schiff base reactions of DA with Pa enhanced the binding ability of TpPa-COF to the PI substrate and improved the interlamellar interaction between the TpPa-COF nanocrystals, which reduced the pore diameter of the membrane. We tracked the in situ synthesis processes for the TpPa-COF and the molecularly soldered pDA/TpPa[water/EtOH (W/E)]-COF membranes for up to 2 hours. Fourier transform infrared spectroscopy results in fig. S1 showed that the pDA/Pa membrane had a peak at ~3277 cm^{-1}, which was the merged peak from amine —N—H and phenolic —OH stretching vibrations of pDA and Pa (*22*). The appearance of a stronger peak at ~2933 cm^{-1} was attributed to the —CH_2— stretching, and the peaks at ~1590 and ~1650 cm^{-1} were due to the —N—H vibration of pDA/Pa and the —C═N bonds between them, respectively. The obtained spectra of the TpPa-COF membrane clearly showed the characteristic —C═C and —C—N stretching bands at 1518 and 1249 cm^{-1}, confirming the occurrence of the Schiff base reaction and successful synthesis of the 2D extended TpPa-COF framework in a keto form on the PI substrates (*17*, *23*, *24*). In addition, the accompanying stretching bands at 1650 and 3277 cm^{-1} indicated the presence of unreacted aldehyde and the amino groups of the Tp and Pa precursors. After adding DA, the intensity of peaks for pDA/TpPa(W/E)-COF membrane at 1650, 1518, and 1249 cm^{-1} increased, which was attributed to the self-polymerization of DA and the covalent reaction of DA with Pa and TpPa-COF. The reaction was further verified by the measurements of elemental composition via x-ray photoelectron spectroscopy (table S1 and fig. S2). The TpPa-COF membrane had 8.25% N with an N/O ratio of 0.42. The N/O ratio of the pDA/TpPa(W/E)-COF membrane increased to 0.73. The oxygen content (45.68%) of Tp ($C_9H_6O_6$) was more than double that of DA (20.89% $C_8H_{11}O_2N$), according to molecule specific formulas. Longer reaction times resulted in the deposition of more DA on the membrane, which greatly increased the N content and the N/O ratio. Concurrently, a large amount of Pa could be anchored on the membrane surface by Schiff base with DA, further increasing the N content and the N/O ratio.

To elucidate the underlying mechanism for in situ molecularly soldered pDA polymerization-assisted COF synthesis, we investigated the reaction kinetics through real-time digital images of incubation solutions (fig. S3). The solutions containing only TpPa-COF turned yellow within 20 min. In contrast, the solutions containing DA and TpPa-COF became yellow within 3 min and then changed to dark yellow beyond 20 min, where dark yellow precipitates were observed after 2 hours, indicating the rapid nucleation of TpPa-COF crystals in the DA water/EtOH solution. X-ray diffraction (fig. S4) of the precipitates further showed that the TpPa-COF and pDA/TpPa(W/E)-COF have a highly crystalline structure and their peak positions match those in previous reports (*24*, *25*). However, the peak intensity for pDA/TpPa(W/E)-COF was slightly lower than that of the TpPa-COF because of the adhesion of pDA to the surface. The decline of the Brunauer-Emmett-Teller–specific surface area also proved this point (fig. S5).

Furthermore, the choice of solvent had an important influence on the reaction of the whole system. In our research, a mixture of water/EtOH (1:1 by volume) was used as the reaction solvent. This dual-solvent system has several advantages: (i) The EtOH is instrumental to the sufficient dissolution of Tp. (ii) The Pa aqueous solution is alkaline, which promotes the self-polymerization of DA and the Schiff base reactions with Pa to strengthen the interlamellar interactions between TpPa-COF nanocrystals. (iii) The generated ROS during the DA polymerization accelerate the nucleophilic reaction of TpPa-COF. The mixed solvent system of water/EtOH can regulate the rate of DA self-polymerization, which could improve the separation performance of the membrane by adjusting its surface structure. For comparison, we adopted the same method separately with pure water and EtOH as the solvents. The membranes formed in the three solvent systems are shown in fig. S6. After 2 hours of reaction, the colors of pDA/TpPa-COF membranes in water [pDA/TpPa(W)-COF], water/EtOH [pDA/TpPa(W/E)-COF], and EtOH [pDA/TpPa(E)-COF] were black, dark green, and yellow green, respectively. For the nanofiltration applications, the pDA/TpPa(W/E)-COF membrane prepared in mixed solvent showed the best performance (Fig. 2A).

Since the self-polymerization of DA was greatly affected by the pH of the reaction media, which, in turn, would affect the formation of the COF, the characteristics and structure of the formed membranes were closely related to the pH value of the solution. Hence, the change in pH of the pDA/TpPa-COF solution as a function of time in different solvent systems was monitored (Fig. 2B). The initial pH of the pDA/TpPa(W)-COF precursor solution was 8.12, which

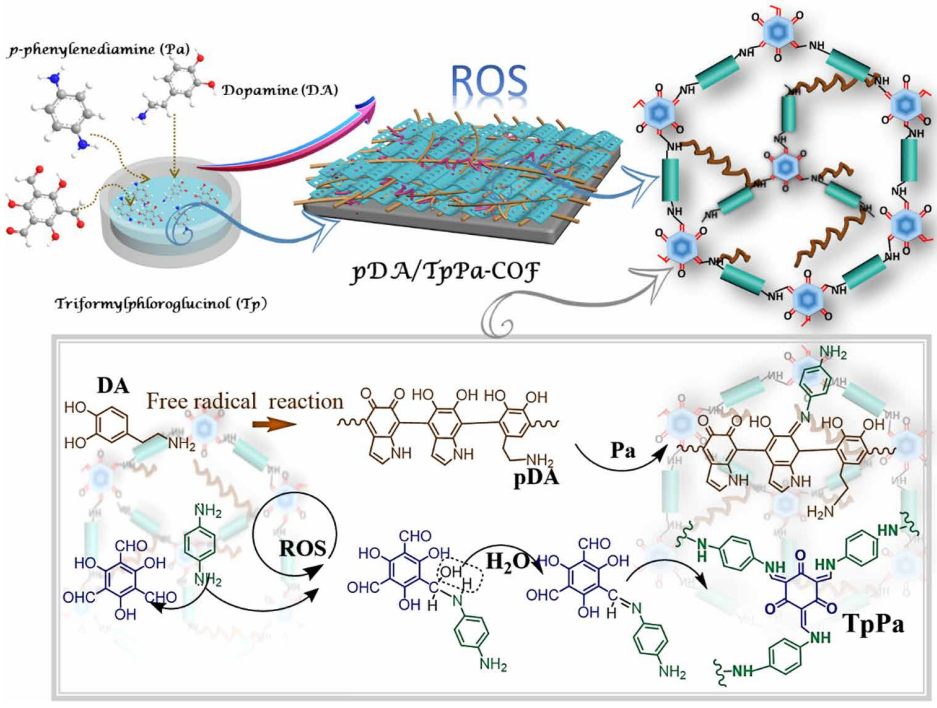

Fig. 1. The process of in situ molecular soldering engineering to fabricate COF membranes.

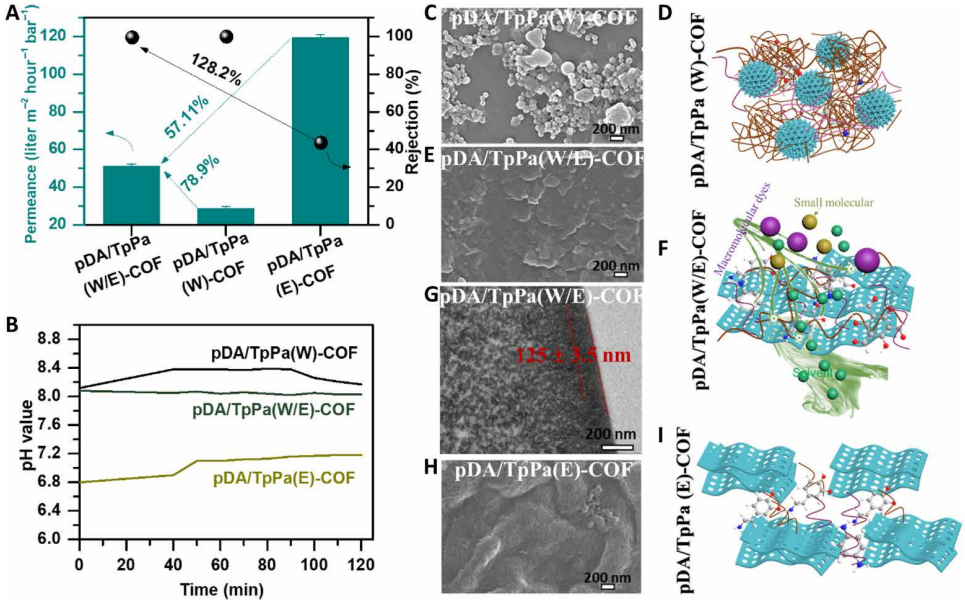

Fig. 2. The effects of different synthesis solvents on pDA/TpPa membrane performance and morphologies and the pH value evolution during the COF formation. (**A**) Membrane permeance and rejection efficiency for Na_2SO_4 including fabrication of pDA/TpPa(W)-COF, pDA/TpPa(W/E)-COF, and pDA/TpPa(E)-COF membranes. (**B**) Real-time pH values of incubation solutions during membrane fabrication process. Scanning electron microscopy (SEM) image of (**C**) pDA/TpPa(W)-COF, (**E**) pDA/TpPa(W/E)-COF, and (**H**) pDA/TpPa(E)-COF membranes. (**G**) Cross-sectional transmission electron microscopy (TEM) image of pDA/TpPa(W/E)-COF membrane. Schematic of membrane structure and separation process of (**D**) pDA/TpPa(W)-COF, (**F**) pDA/TpPa(W/E)-COF, and (**I**) pDA/TpPa(E)-COF membranes.

increased to 8.38 in 40 min, and remained unchanged for approximately 50 min. The first increase in pH should be due to the nucleation of COF, accompanied by the formation of COF oligomers/polymers, while the point of pH drop can be attributed to the crystallization of the amorphous part of the COF and the proton release during DA polymerization (*12*, *26*). This pH range was conducive for DA aggregation. Because of the rapid polymerization of DA at this pH, significant amounts of ROS were generated, promoting the rapid nucleation of TpPa-COF in water, resulting the deposition of more pDA on the membrane surface. Therefore, spherical nanoparticles

were formed (fig. S7A), which settled in and clogged the membrane pores, and blocked the passage of Na_2SO_4 (Fig. 2, C and D). As a result, the pDA/TpPa(W)-COF membrane had a low Na_2SO_4 permeance (28.7 liter m^{-2} $hour^{-1}$ bar^{-1}) with a small pore size (fig. S8), dense membrane structure, thick selective layer, and high surface roughness of 12.5 nm (figs. S9A and S10A). For pDA/TpPa(W/E)-COF, the initial pH of the precursor solution was ~8.08, which is slightly lower than that of the pDA/TpPa(W)-COF solution because of the low pK_a (where K_a is the acid dissociation constant) of EtOH. The pH value remained unchanged (from 8.08 to 8.03) within 120 min (Fig. 2B). The nucleation rate of TpPa-COF in water/EtOH was slower as compared to identical reactions in water solutions, as the promotion effect of ROS on the TpPa-COF nucleophilic reaction was weakened. In this pH range, DA could also polymerize and generate ROS but below the self-polymerization capacity in the water system. As a result, a lamellar sandwich layer of the pDA/TpPa(W/E)-COF membrane was formed (Fig. 2E and fig. S7B). Therefore, pDA/TpPa(W/E)-COF membrane exhibited a high Na_2SO_4 permeance of 51.3 liter m^{-2} $hour^{-1}$ bar^{-1} and 99.5% Na_2SO_4 rejection. The precise pore size of this membrane was obtained (Fig. 2F and fig. S8), and the membrane comprised a 125 ± 3.5 nm thin-selective layer (Fig. 2G), exhibiting a low surface roughness of 3.92 nm (fig. S10B). In the pDA/TpPa(E)-COF solution, the pH increased from 6.80 to 7.18 during the reaction. This lower pH range enabled the self-assembly of 2D layered TpPa-COFs but not DA polymerization, causing a marked reduction in Na_2SO_4 rejection (43.6%). The large pore and loose delamination structure (Fig. 2, H and I, and figs. S7C, S8, S9B, and S10C) are the main causes of its poor rejection rate. Room-temperature electron paramagnetic resonance spectra for the free radical test proved the above points of view (fig. S11). An obvious low-bandgap single-line spectrum was detected for pDA/TpPa(W)-COF, consistent with the presence of semiquinone radicals (*27*, *28*). pDA/TpPa(W/E)-COF exhibited similar spectral shapes, but the resonance signals were relatively weak. In addition, no semiquinone radical species were detected in pDA/TpPa(E)-COF. These results demonstrated that DA in different solvents had different polymerization strengths with different amounts of ROS being generated, which was critical for the in situ molecularly soldered COF membrane formation. As a result, we chose a mixture of EtOH and water as the solvent for the reaction.

pDA was crucial for the in situ molecularly soldered pDA/TpPa-COF into a defect-free membrane demonstrating excellent separation performance. It is extensively recognized that the catechol group of DA can be easily oxidized to quinone under alkaline/aqueous condition. After a series of oxidation, cyclization, and further rearrangement reactions, a vital metastable intermediate (5,6-dihydroxy-indole) is formed, which can react with its oxidized form (e.g., indolequinone) by generating semiquinone radicals through dismutation. These radicals can be readily reoxidized by O_2 with the concomitant formation of ROS ($O_2^{\bullet-}$) and the *o*-quinone of DA (fig. S12) (*29*–*33*). Subsequently, the self-polymerization of DA took place through a radical-induced intramolecular cross-linking pathway. To further elucidate the mechanism underlying the formation of TpPa-COF assisted by the ROS, we performed density functional theory (DFT) simulations of the reactions between Pa and Tp molecules with and without ROS. The mechanism of the conventional synthesis process is illustrated by path I in Fig. 3, which describes the formation of a C—N bond through an intermediate C1. This stage had an energy

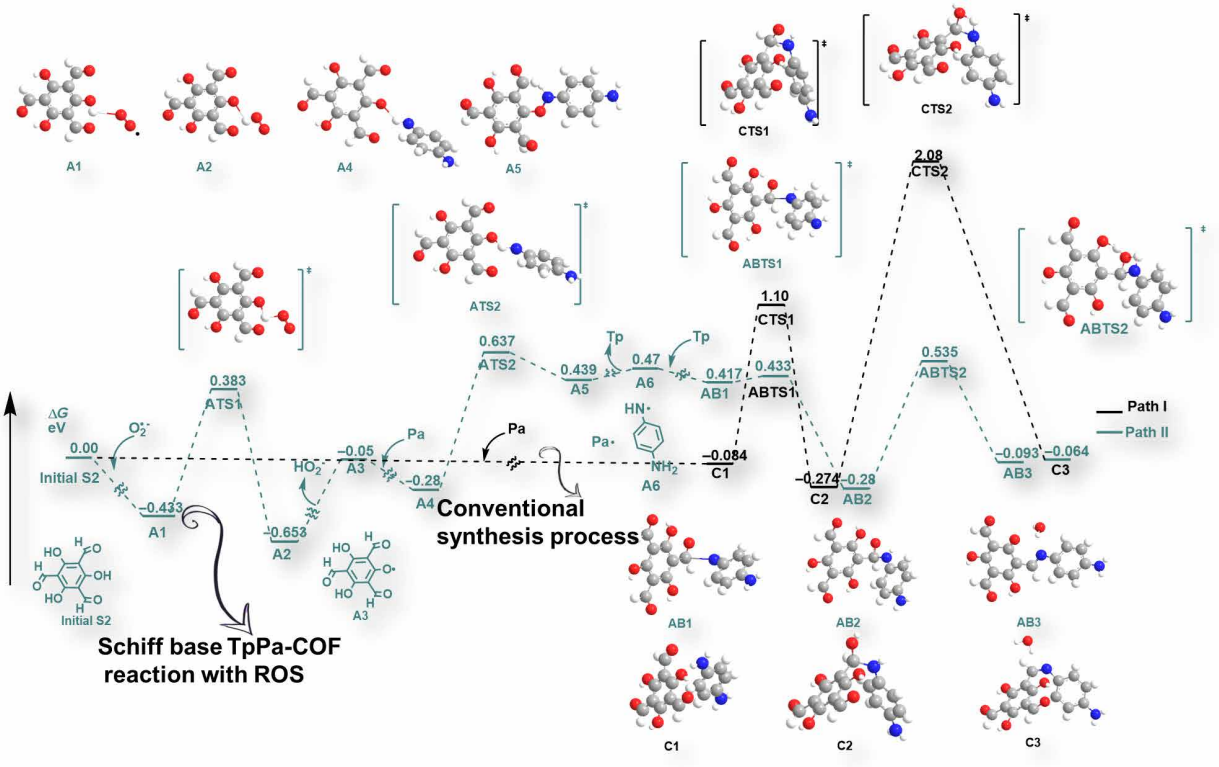

Fig. 3. DFT calculation for the reaction between Pa and Tp molecules with and without ROS.

barrier (Ea) of 1.184 eV. Further dehydration of C2 led to the formation of the TpPa-COF as a Schiff base. The rate-limiting step of the whole reaction was C—N bond formation (*34*). In the presence of DA, reactive oxygen free radicals were generated during the self-polymerization. The DFT simulation of the reactions between Tp and a free radical–produced imino radical (Pa·) was performed as a simplified model. These calculations demonstrated a significant reduction in Ea for the rate-limiting step (0.683 eV versus 1.184 eV) and the dehydration of the amino radical (0.815 eV versus 2.354 eV) for the formation of TpPa-COF Schiff base, as shown in path II of Fig. 3. The simulation calculations also suggested that the ROS generated by the self-polymerization of DA was essential for the rapid TpPa-COF synthesis. Without ROS, the reaction of the Schiff base TpPa-COF needs to overcome a larger energy barrier. Consequently, pDA was crucial to the formation of a high-performance pDA/TpPa(W/E)-COF membrane. The pDA not only could quickly react with Pa at room temperature for improved distribution and much higher loading of COF-TpPa on the surface of the developed membrane but also reduced the effective sieving pore diameter of the membrane and improved the interlamellar interaction between TpPa-COF nanocrystals and accelerated TpPa-COF nucleophilic reactions.

To validate the importance of pDA, we synthesized a series of pDA/TpPa(W/E)-COF membranes at various DA concentration and reaction times. With an increase in the DA concentration, the membrane thickness increased and the surface pore aperture size gradually decreased (figs. S13 and S14), resulting in a gradual decrease in membrane permeance and an increase in rejection. This was ascribed to the generation of more ROS with a high dose of pDA, which boosted the deposition of TpPa-COF and resulted in more pDA chains settled on the membrane surface (*26*). Furthermore, DA can react with more Pa. The above synergy jointly regulated the structure and desalination performance of the COF membrane. For prolonged reactions, the permeance of the pDA/TpPa(W/E)-COF membrane decreased (fig. S15A). The typical TpPa-COF nucleation process was accelerated because of DA aggregation and covalent reactions. The color of the pDA/TpPa(W/E)-COF membrane gradually deepened from yellow to dark green over time, owing to the deposition of a greater amount of pDA (fig. S15B). By balancing the realization of permeance and rejection, a DA concentration of 0.2 weight % (wt %) and 2 hours of incubation was taken as the optimum reaction condition.

To elucidate the importance of Pa, we fabricated and characterized the structural characteristics of membranes comprising pDA, pDA/Pa, pDA/Tp, TpPa-COF, and pDA/TpPa(W/E)-COF. Ascribing to poor reactivity in water/EtOH, pDA and pDA/Tp coating layers had almost the same thickness and surface roughness (fig. S16, A to D). The introduction of Pa into the pDA coating system increased the pH, and therefore, the DA could react with Pa through Schiff base reaction to form a thicker selective layer (fig. S16E) (*35*). Correspondingly, numerous nanostructured papillae were observed on the surface of the pDA/Pa membrane, and thus, a higher roughness (7.15 nm) was obtained (fig. S16F) (*36*, *37*). It was astonishing that the structure of the membrane changed significantly with and without DA. After the growth of TpPa-COF microcrystals, the pDA/TpPa(W/E)-COF membrane showed a rough sandwich structure. In comparison, without the addition of DA, TpPa-COF nanocrystallites formed loose defective structures in the selective layer of the TpPa-COF membrane (Fig. 4, A and B, and fig. S17). This defective membrane structure was probably due to insufficient nucleation sites, which led to an inferior homogeneous nucleation of TpPa-COF and weak interlamellar interaction between the TpPa-COF nanocrystals. The membranes were analyzed via transmission electron microscopy (TEM) to acquire the precise thickness of the selective layer. As shown in Fig. 2G, the pDA/TpPa(W/E)-COF membrane has an ultrathin selective layer of ~125 nm, which is considerably thinner than those of the mostly reported metal-organic framework and COF membranes (*11*, *15*, *25*). Moreover, no clear boundaries were observed between the underlying substrate and the separation layer for the pDA/TpPa(W/E)-COF membrane, suggesting their tight connection. The concentration of Pa also affected the membrane separation performance, and 2 wt % of Pa was chosen as the optimum addition amount (fig. S18).

In addition, the structure of the membranes studied here notable influenced the surface wettability and charge. The water contact angle (WCA) of the TpPa-COF membrane was smaller than that of the pDA/Pa membrane (fig. S19). Water droplets completely wetted the TpPa-COF membrane within 15 s, suggesting that TpPa-COF demonstrates greater hydrophilicity due to the presence of residual hydrophilic amines and hydroxyl groups in the microporous pore structure (*38*, *39*). A similar phenomenon occurred on the surface of the pDA/TpPa(W/E)-COF membranes, where the WCA was reduced from 19.1° to 0° within 50 s. This fast penetration of water indicated the excellent surface hydrophilicity of the designed membrane and low mass transfer resistance, which was beneficial for fabricating high permeance membranes. In addition, the TpPa-COF and pDA/TpPa(W/E)-COF membranes demonstrated a high water adsorption capacity owing to the layered structures and permanent porosity (fig. S20). As shown in fig. S21, all the membranes were negatively charged in a neutral pH environment. As a result, the ultrathin and hydrophilic pDA/TpPa(W/E)-COF membrane showed ultrahigh Na_2SO_4 permeance of 51.3 liter m^{-2} $hour^{-1}$ bar^{-1}, which was 32.6% higher than that of the pDA/Pa membrane (38.7 liter m^{-2} $hour^{-1}$ bar^{-1}). It also exhibited a high rejection of 99.5% to Na_2SO_4, representing a 186.7% increase when compared to the TpPa-COF membrane (34.7%) (Fig. 4C). Note that this nanofiltration performance surpasses that of state-of-the-art membranes (Fig. 4D and table S2) (*4*, *38*, *40*–*44*).

To further evaluate membrane desalination performance, the pDA/TpPa(W/E)-COF membrane was tested at 5 bar using various inorganic salts with a concentration of 1000 parts per million as the feed (Fig. 4E). The rejection decreased in the order of Na_2SO_4 (99.5%) > $MgSO_4$ (91.3%) > $MgCl_2$ (70.3%) > NaCl (49.2%). The hydration radii of Na^+, Cl^-, SO_4^{2-}, and Mg^{2+} were all larger than the pore size of the pDA/TpPa(W/E)-COF membrane (*45*). Nevertheless, because of the broad pore size distribution and the small hydration radii of Cl^-, the ion rejection rates for $MgCl_2$ and NaCl were relatively low. The separation mechanism of the membranes was dominated by a size-sieving/Donnan exclusion collaborative effect (*46*). The surface of the pDA/TpPa(W/E)-COF membrane was negatively charged; therefore, the Donnan repulsion effect for SO_4^{2-} was stronger than that for Cl^-, and the hydration radius of Cl^- was smaller than that of SO_4^{2-} (*47*). As a result, high rejection of SO_4^{2-} and low rejection of Cl^- were obtained. Therefore, the pDA/TpPa(W/E)-COF membrane had a superior mono/bivalent salt selectivity, surpassing that of most of the established desalination membranes (Fig. 4F) (*44*, *48*–*58*). Such superior performance mainly resulted from the water transport channels formed in 2D COF membrane. This outstanding performance demonstrated the high competence of the in

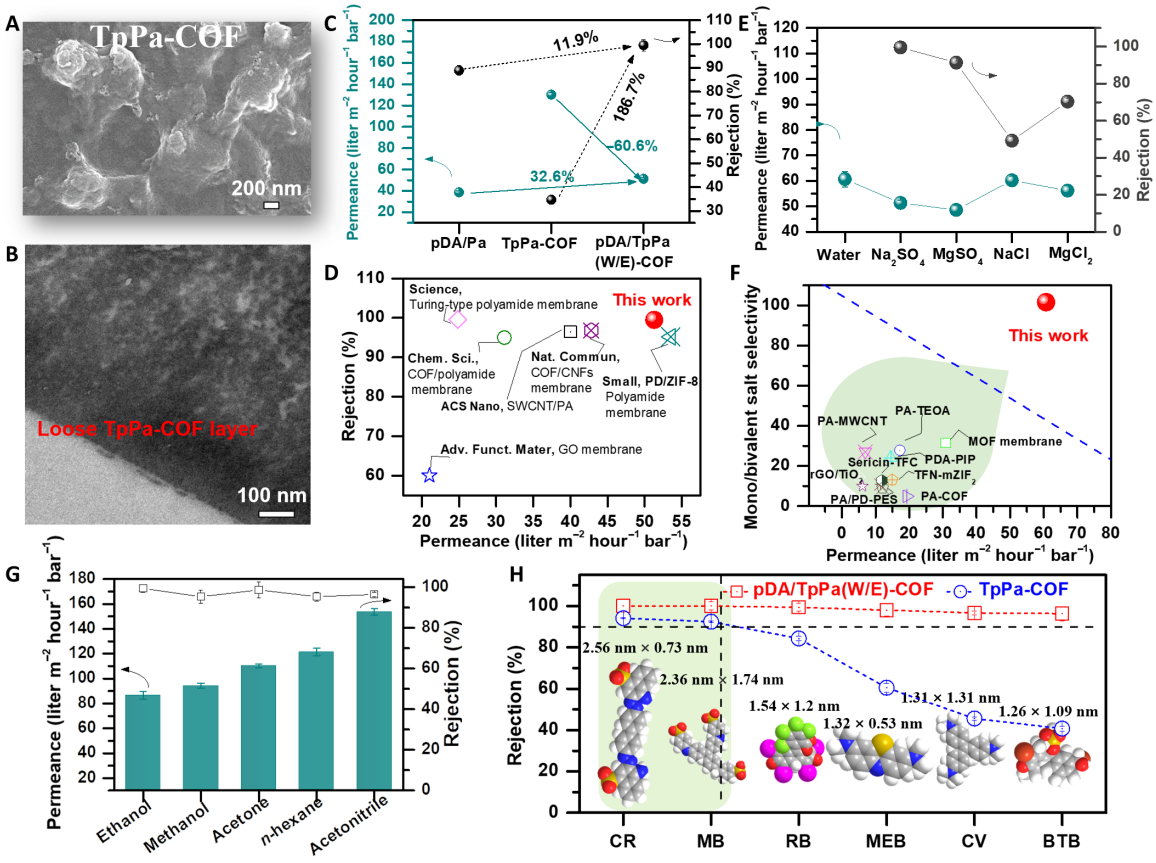

Fig. 4. The morphology of TpPa-COF membrane synthesized under W/E solvent and the separation performance comparison of optimized pDA/TpPa-COF (W/E) membrane for salt solution or dyes/organic solvent system. (**A**) SEM and (**B**) TEM image of TpPa-COF membrane. (**C**) Permeance and rejection of pDA/TpPa(W/E)-COF, TpPa-COF, and pDA/Pa membrane for separating Na_2SO_4. (**D**) Performance comparison of pDA/TpPa(W/E)-COF membrane with the state-of-the-art membranes for separating Na_2SO_4. (**E**) Salt separation performance of pDA/TpPa(W/E)-COF membrane. (**F**) Trade-off between water permeance and mono/bivalent selectivity of NF membranes and the state-of-the-art membranes. The red circle represents as-prepared membrane in this work. MOF, metal-organic framework. (**G**) The separation performance of pDA/TpPa(W/E)-COF membrane for Congo red in different organic solvents. (**H**) The rejection of pDA/TpPa(W/E)-COF and TpPa-COF membrane for different dyes in EtOH.

situ molecularly soldered pDA/TpPa(W/E)-COF membranes in mono/bivalent salt discrimination. The in situ molecularly soldered strategy can also be extended to diverse polyphenols (i.e., gallic acid and tannic acid) (fig. S22).

In addition, biofouling is a common reason for performance degradation due to the accumulation of biomaterials on the membrane surface. Schiff base reaction materials have shown excellent antipollution ability, and thus, the antifouling properties of the pDA/TpPa(W/E)-COF membrane were further studied using bovine serum albumin (BSA) and humic acid (HA) as the probe foulants. The flux recovery ratios of the pDA/TpPa(W/E)-COF membrane for BSA and HA separations after three cycles were 98.4 and 94.0%, respectively, with complete rejection and lower total fouling ratio ($\boldsymbol{DR}_t$) (2.8% for BSA and 10% for HA; figs. S23 and S24) (*59*, *60*). The excellent resistance to hydrophobic biomolecule adhesion was attributed to the hydrophilic character of the negatively charged pDA/TpPa(W/E)-COF membrane. Furthermore, the Donnan exclusion mechanism can also contribute to the excellent antibiofouling characteristics because both BSA and HA molecules were negatively charged. The performance stability of the pDA/TpPa(W/E)-COF membrane was also verified over time, and there was no obvious change in permeance and rejection (fig. S25). Furthermore, we also evaluated the mechanical and thermal stabilities of the as-prepared TpPa-COF and pDA/TpPa(W/E)-COF membranes. As shown in fig. S26, the pDA/TpPa(W/E)-COF membranes showed much higher tensile strength than the TpPa-COF membrane, underpinned 33.6% of the increment, from 13.1 ± 0.2 to 17.5 ± 0.5 MPa. The good mechanical properties of the pDA/TpPa(W/E)-COF membranes were mainly due to the multiple covalent reactions of pDA with Pa and TpPa-COF (*4*). The TpPa-COF membrane, the interlamellar weak π-π interactions, van der Waals force, and hydrogen bonding interactions made it fragile under stretching. Moreover, thermogravimetric analysis curves showed that the membrane had good thermal stability (fig. S27). The solvent stability of the membrane in various solvents was also studied using different sizes and charges of dyes as the solutes. The pDA/TpPa(W/E)-COF membrane demonstrated excellent separation performance for organic solvent nanofiltration (Fig. 4G). The permeances for all the solvents were higher than 86 liter m^{-2} hour^{-1} bar^{-1}, and the rejections of various dyes surpassed 95%. In comparison, the TpPa-COF membrane showed a relatively low rejection of dyes with a molecular size smaller than 2 nm (Fig. 4H), and the rejections of various organic solvents declined for the 120-hour test (fig. S28)

because of the weak interlamellar interactions between the TpPa-COF nanocrystals. In contrast, no appreciable changes were observed in the permeance and rejection of the pDA/TpPa(W/E)-COF membrane (fig. S29), which verified the strong structural stability and demonstrated the applicability of the pDA/TpPa(W/E)-COF membrane for filtration in various organic solvent systems. To eliminate the influence of adsorption on the separation performance, direct evidence was provided by the evaluating percentage of adsorbed dyes, which indicated the low adsorption for all the dyes (fig. S30) (*59*). Therefore, it was reasonable to conclude that the high rejection of the pDA/TpPa(W/E)-COF membrane was dominated by size exclusion and electrostatic interaction. Therefore, the advanced approaches developed in this work can simultaneously realize the effective pore size manipulation, mechanical strength enhancement, and durability reinforcement of COF membranes, which would be significantly beneficial for improving the practical application potential of COF membranes.

DISCUSSION

We demonstrated an in situ molecularly soldered strategy for the facile construction of ultrafast, precise-sieving, ultrathin, and defect-free pDA/TpPa(W/E)-COF membranes, exhibiting excellent antifouling properties and superior structural stability for both desalination and organic solvent nanofiltration by using analogous chemical environments for COF synthesis and DA polymerization at room temperature. DFT simulation and complementary experiments clarified that the ROS generated during DA self-polymerization can prominently accelerate the nucleophilic reactions of COF to regulate the surface structure and pore size of molecularly soldered COF membranes. The brand-new pDA/TpPa(W/E)-COF membranes showed remarkable competence in mono/bivalent salt separation, high antipollution capacity, and precise separation of diverse small molecules. The pDA/TpPa(W/E)-COF membranes demonstrated a permeance of 53.1 liter m^{-2} $hour^{-1}$ bar^{-1} and 99.5% rejection of Na_2SO_4, which are much superior to that of state-of-the-art membranes. The pDA/TpPa(W/E)-COF membranes also exhibited superior stability in a wide variety of organic solvents, displaying robust mechanical strength and excellent durability in long-term filtration. The simplicity of the membrane fabrication process potentially enables the large-scale production of durable high-performance COF membranes for crucial energy-efficient separations to tackle the ever-increasing energy and environmental issues.

MATERIALS AND METHODS

Preparation of TpPa-COF and pDA/TpPa(W/E)-COF membranes

To prepare pDA/TpPa(W/E)-COF membranes, 2 g of Pa was dissolved in 50 ml of deionized water. Then, 0.2 g of DA hydrochloride was dissolved in a Pa aqueous solution via ultrasonic treatment for 10 min, and 0.05 g of Tp was dissolved in 50 ml of EtOH. These two solutions were poured into the beaker simultaneously and stirred for 10 s. Afterward, the PI substrate was immersed in the solution and kept reaction different durations at ambient temperature and light. Last, the membrane was washed thrice with water and then dried under a dynamic vacuum at 120°C for 2 hours. For the TpPa-COF, pDA/TpPa(W)-COF, and pDA/TpPa(E)-COF membranes, we used the same method as above using different solvents.

SUPPLEMENTARY MATERIALS

Supplementary material for this article is available at http://advances.sciencemag.org/cgi/content/full/7/13/eabe8706/DC1

REFERENCES AND NOTES

1. D. S. Sholl, R. P. Lively, Seven chemical separations to change the world. *Nature* **532**, 435–437 (2016).
2. World Health Organization, United Nations Children's Fund, "Water, sanitation, hygiene, and waste management for the COVID-19 virus: Interim guidance, 23 April 2020" (World Health Organization, 2020).
3. M. S. Mauter, I. Zucker, F. O. Perreault, J. R. Werber, J.-H. Kim, M. Elimelech, The role of nanotechnology in tackling global water challenges. *Nat. Sustain.* **1**, 166–175 (2018).
4. H. Yang, L. Yang, H. Wang, Z. Xu, Y. Zhao, Y. Luo, N. Nasir, Y. Song, H. Wu, F. Pan, Z. Jiang, Covalent organic framework membranes through a mixed-dimensional assembly for molecular separations. *Nat. Commun.* **10**, 2101 (2019).
5. H. B. Park, J. Kamcev, L. M. Robeson, M. Elimelech, B. D. Freeman, Maximizing the right stuff: The trade-off between membrane permeability and selectivity. *Science* **356**, eaab0530 (2017).
6. N. C. Su, D. T. Sun, C. M. Beavers, D. K. Britt, W. L. Queen, J. J. Urban, Enhanced permeation arising from dual transport pathways in hybrid polymer–MOF membranes. *Energ. Environ. Sci.* **9**, 922–931 (2016).
7. H. Zhang, Q. He, J. Luo, Y. Wan, S. B. Darling, Sharpening nanofiltration: Strategies for enhanced membrane selectivity. *ACS Appl. Mater. Interfaces* **12**, 39948–39966 (2020).
8. K. Dey, M. Pal, K. C. Rout, S. Kunjattu H, A. Das, R. Mukherjee, U. K. Kharul, R. Banerjee, Selective molecular separation by interfacially crystallized covalent organic framework thin films. *J. Am. Chem. Soc.* **139**, 13083–13091 (2017).
9. H. Wang, Z. Zeng, P. Xu, L. Li, G. Zeng, R. Xiao, Z. Tang, D. Huang, L. Tang, C. Lai, D. Jiang, Y. Liu, H. Yi, L. Qin, S. Ye, X. Ren, W. Tang, Recent progress in covalent organic framework thin films: Fabrications, applications and perspectives. *Chem. Soc. Rev.* **48**, 488–516 (2019).
10. S. Kim, H. Wang, Y. M. Lee, 2D nanosheets and their composite membranes for water, gas, and ion separation. *Angew. Chem. Int. Ed.* **58**, 17512–17527 (2019).
11. S. Kandambeth, B. P. Biswal, H. D. Chaudhari, K. C. Rout, S. Kunjattu H, S. Mitra, S. Karak, A. Das, R. Mukherjee, U. K. Kharul, Selective molecular sieving in self-standing porous covalent-organic-framework membranes. *Adv. Mater.* **29**, 1603945 (2017).
12. X. H. Liu, C. Z. Guan, D. Wang, L. J. Wan, Graphene-like single-layered covalent organic frameworks: Synthesis strategies and application prospects. *Adv. Mater.* **26**, 6912–6920 (2014).
13. C. R. DeBlase, K. Hernández-Burgos, K. E. Silberstein, G. G. Rodríguez-Calero, R. P. Bisbey, H. D. Abruña, W. R. Dichtel, Rapid and efficient redox processes within 2D covalent organic framework thin films. *ACS Nano* **9**, 3178–3183 (2015).
14. J. Fu, S. Das, G. Xing, T. Ben, V. Valtchev, S. Qiu, Fabrication of COF-MOF composite membranes and their highly selective separation of H_2/CO_2. *J. Am. Chem. Soc.* **138**, 7673–7680 (2016).
15. H. Fan, J. Gu, H. Meng, A. Knebel, J. Caro, High-flux membranes based on the covalent organic framework COF-LZU1 for selective dye separation by nanofiltration. *Angew. Chem. Int. Ed.* **57**, 4083–4087 (2018).
16. M. Matsumoto, L. Valentino, G. M. Stiehl, H. B. Balch, A. R. Corcos, F. Wang, D. C. Ralph, B. J. Mariñas, W. R. Dichtel, Lewis-acid-catalyzed interfacial polymerization of covalent organic framework films. *Chem* **4**, 308–317 (2018).
17. Q. Hao, C. Zhao, B. Sun, C. Lu, J. Liu, M. Liu, L.-J. Wan, D. Wang, Confined synthesis of two-dimensional covalent organic framework thin films within superspreading water layer. *J. Am. Chem. Soc.* **140**, 12152–12158 (2018).
18. Y. Ying, D. Liu, J. Ma, M. Tong, W. Zhang, H. Huang, Q. Yang, C. Zhong, A GO-assisted method for the preparation of ultrathin covalent organic framework membranes for gas separation. *J. Mater. Chem. A* **4**, 13444–13449 (2016).
19. H. C. Yang, R. Z. Waldman, M. B. Wu, J. Hou, L. Chen, S. B. Darling, Z.-K. Xu, Dopamine: Just the right medicine for membranes. *Adv. Funct. Mater.* **28**, 1705327 (2018).
20. H. Lee, S. M. Dellatore, W. M. Miller, P. B. Messersmith, Mussel-inspired surface chemistry for multifunctional coatings. *Science* **318**, 426–430 (2007).
21. Z. Wang, H. C. Yang, F. He, S. Peng, Y. Li, L. Shao, S. B. Darling, Mussel-inspired surface engineering for water-remediation materials. *Matter* **1**, 115–155 (2019).
22. J. Zhao, C. Fang, Y. Zhu, G. He, F. Pan, Z. Jiang, P. Zhang, X. Cao, B. Wang, Manipulating the interfacial interactions of composite membranes via a mussel-inspired approach for enhanced separation selectivity. *J. Mater. Chem. A* **3**, 19980–19988 (2015).
23. R. Wang, X. Shi, Z. Zhang, A. Xiao, S.-P. Sun, Z. Cui, Y. Wang, Unidirectional diffusion synthesis of covalent organic frameworks (COFs) on polymeric substrates for dye separation. *J. Membr. Sci.* **586**, 274–280 (2019).
24. B. P. Biswal, S. Chandra, S. Kandambeth, B. Lukose, T. Heine, R. Banerjee, Mechanochemical synthesis of chemically stable isoreticular covalent organic frameworks. *J. Am. Chem. Soc.* **135**, 5328–5331 (2013).

25. R. Wang, X. Shi, A. Xiao, W. Zhou, Y. Wang, Interfacial polymerization of covalent organic frameworks (COFs) on polymeric substrates for molecular separations. *J. Membr. Sci.* **566**, 197–204 (2018).
26. J. Liu, F. Yang, L. Cao, B. Li, K. Yuan, S. Lei, W. Hu, A robust nonvolatile resistive memory device based on a freestanding ultrathin 2D imine polymer film. *Adv. Mater.* **31**, 1902264 (2019).
27. G. Ulas, T. Lemmin, Y. Wu, G. T. Gassner, W. F. DeGrado, Designed metalloprotein stabilizes a semiquinone radical. *Nat. Chem.* **8**, 354–359, 359 (2016).
28. O. Z. Fisher, B. L. Larson, P. S. Hill, D. Graupner, M. T. Nguyen-Kim, N. S. Kehr, L. De Cola, R. Langer, D. G. Anderson, Melanin-like hydrogels derived from gallic macromers. *Adv. Mater.* **24**, 3032–3036 (2012).
29. Y. Song, G. R. Buettner, Thermodynamic and kinetic considerations for the reaction of semiquinone radicals to form superoxide and hydrogen peroxide. *Free Radic. Bio. Med.* **49**, 919–962 (2010).
30. X. Yuan, A. N. Pham, C. J. Miller, T. D. Waite, Copper-catalyzed hydroquinone oxidation and associated redox cycling of copper under conditions typical of natural saline waters. *Environ. Sci. Technol.* **47**, 8355–8364 (2013).
31. F. Yu, S. Chen, Y. Chen, H. Li, L. Yang, Y. Chen, Y. Yin, Experimental and theoretical analysis of polymerization reaction process on the polydopamine membranes and its corrosion protection properties for 304 stainless steel. *J. Mol. Struct.* **982**, 152–161 (2010).
32. A. N. Pham, T. D. Waite, Cu(II)-catalyzed oxidation of dopamine in aqueous solutions: Mechanism and kinetics. *J. Inorg. Biochem.* **137**, 74–84 (2014).
33. J. Segura-Aguilar, C. Lind, On the mechanism of the Mn^{3+}-induced neurotoxicity of dopamine: Prevention of quinone-derived oxygen toxicity by DT diaphorase and superoxide dismutase. *Chem. Biol. Interact.* **72**, 309–324 (1989).
34. M. Zhang, J. Chen, S. Zhang, X. Zhou, L. He, M. V. Sheridan, M. Yuan, M. Zhang, L. Chen, X. Dai, F. Ma, J. Wang, J. Hu, G. Wu, X. Kong, R. Zhou, T. E. Albrecht-Schmitt, Z. Chai, S. Wang, Electron beam irradiation as a general approach for the rapid synthesis of covalent organic frameworks under ambient conditions. *J. Am. Chem. Soc.* **142**, 9169–9174 (2020).
35. X. You, H. Wu, Y. Su, J. Yuan, R. Zhang, Q. Yu, M. Wu, Z. Jiang, X. Cao, Precise nanopore tuning for a high-throughput desalination membrane via co-deposition of dopamine and multifunctional POSS. *J. Mater. Chem. A* **6**, 13191–13202 (2018).
36. M. B. M. Y. Ang, Y. L. Ji, S. H. Huang, K. R. Lee, J.-Y. Lai, A facile and versatile strategy for fabricating thin-film nanocomposite membranes with polydopamine-piperazine nanoparticles generated in situ. *J. Membr. Sci.* **579**, 79–89 (2019).
37. M. A. Rahim, M. Björnmalm, N. Bertleff-Zieschang, Q. Besford, S. Mettu, T. Suma, M. Faria, F. Caruso, Rust-mediated continuous assembly of metal–phenolic networks. *Adv. Mater.* **29**, 1606717 (2017).
38. Z. Zhang, X. Shi, R. Wang, A. Xiao, Y. Wang, Ultra-permeable polyamide membranes harvested by covalent organic framework nanofiber scaffolds: A two-in-one strategy. *Chem. Sci.* **10**, 9077–9083 (2019).
39. X. Zhang, H. Li, J. Wang, D. Peng, J. Liu, Y. Zhang, In-situ grown covalent organic framework nanosheets on graphene for membrane-based dye/salt separation. *J. Membr. Sci.* **581**, 321–330 (2019).
40. Y. Han, Z. Xu, C. Gao, Ultrathin graphene nanofiltration membrane for water purification. *Adv. Funct. Mater.* **23**, 3693–3700 (2013).
41. Y. Zhu, W. Xie, S. Gao, F. Zhang, W. Zhang, Z. Liu, J. Jin, Single-walled carbon nanotube film supported nanofiltration membrane with a nearly 10 nm thick polyamide selective layer for high-flux and high-rejection desalination. *Small* **12**, 5034–5041 (2016).
42. Z. Wang, Z. Wang, S. Lin, H. Jin, S. Gao, Y. Zhu, J. Jin, Nanoparticle-templated nanofiltration membranes for ultrahigh performance desalination. *Nat. Commun.* **9**, 2004 (2018).
43. Z. Tan, S. Chen, X. Peng, L. Zhang, C. Gao, Polyamide membranes with nanoscale turing structures for water purification. *Science* **360**, 518–521 (2018).
44. S. Gao, Y. Zhu, Y. Gong, Z. Wang, W. Fang, J. Jin, Ultrathin polyamide nanofiltration membrane fabricated on brush-painted single-walled carbon nanotube network support for ion sieving. *ACS Nano* **13**, 5278–5290 (2019).
45. X. Liu, N. K. Demir, Z. Wu, K. Li, Highly water-stable zirconium metal–organic framework UiO-66 membranes supported on alumina hollow fibers for desalination. *J. Am. Chem. Soc.* **137**, 6999–7002 (2015).
46. X. You, H. Wu, R. Zhang, Y. Su, L. Cao, Q. Yu, J. Yuan, K. Xiao, M. He, Z. Jiang, Metal-coordinated sub-10 nm membranes for water purification. *Nat. Commun.* **10**, 4160 (2019).
47. P. Marchetti, M. F. Jimenez Solomon, G. Szekely, A. G. Livingston, Molecular separation with organic solvent nanofiltration: A critical review. *Chem. Rev.* **114**, 10735–10806 (2014).
48. M. Safarpour, V. Vatanpour, A. Khataee, M. Esmaeili, Development of a novel high flux and fouling-resistant thin film composite nanofiltration membrane by embedding reduced graphene oxide/TiO_2. *Sep. Purif. Technol.* **154**, 96–107 (2015).
49. J. Zhu, L. Qin, A. Uliana, J. Hou, J. Wang, Y. Zhang, X. Li, S. Yuan, J. Li, M. Tian, J. Lin, B. Van der Bruggen, Elevated performance of thin film nanocomposite membranes enabled by modified hydrophilic MOFs for nanofiltration. *ACS Appl. Mater. Interfaces* **9**, 1975–1986 (2017).
50. C. Wang, Z. Li, J. Chen, Z. Li, Y. Yin, L. Cao, Y. Zhong, H. Wu, Covalent organic framework modified polyamide nanofiltration membrane with enhanced performance for desalination. *J. Membr. Sci.* **523**, 273–281 (2017).
51. S.-M. Xue, Z.-L. Xu, Y.-J. Tang, C.-H. Ji, Polypiperazine-amide nanofiltration membrane modified by different functionalized multiwalled carbon nanotubes (MWCNTs). *ACS Appl. Mater. Interfaces* **8**, 19135–19144 (2016).
52. J. Zhu, S. Yuan, A. Uliana, J. Hou, J. Li, X. Li, M. Tian, Y. Chen, A. Volodin, B. Van der Bruggen, High-flux thin film composite membranes for nanofiltration mediated by a rapid co-deposition of polydopamine/piperazine. *J. Membr. Sci.* **554**, 97–108 (2018).
53. Y. Li, Y. Su, J. Li, X. Zhao, R. Zhang, X. Fan, J. Zhu, Y. Ma, Y. Liu, Z. Jiang, Preparation of thin film composite nanofiltration membrane with improved structural stability through the mediation of polydopamine. *J. Membr. Sci.* **476**, 10–19 (2015).
54. C. Zhou, Y. Shi, C. Sun, S. Yu, M. Liu, C. Gao, Thin-film composite membranes formed by interfacial polymerization with natural material sericin and trimesoyl chloride for nanofiltration. *J. Membr. Sci.* **471**, 381–391 (2014).
55. L.-F. Liu, X. Huang, X. Zhang, K. Li, Y.-L. Ji, C. Y. Yu, C.-J. Gao, Modification of polyamide TFC nanofiltration membrane for improving separation and antifouling properties. *RSC Adv.* **8**, 15102–15110 (2018).
56. F. Yan, H. Chen, Y. Lü, Z. Lü, S. Yu, M. Liu, C. Gao, Improving the water permeability and antifouling property of thin-film composite polyamide nanofiltration membrane by modifying the active layer with triethanolamine. *J. Membr. Sci.* **513**, 108–116 (2016).
57. J. Zhu, J. Hou, S. Yuan, Y. Zhao, Y. Li, R. Zhang, M. Tian, J. Li, J. Wang, B. Van der Bruggen, MOF-positioned polyamide membranes with a fishnet-like structure for elevated nanofiltration performance. *J. Mater. Chem. A* **7**, 16313–16322 (2019).
58. Z. Yang, Z. W. Zhou, H. Guo, Z. Yao, X. H. Ma, X. Song, S. P. Feng, C. Y. Tang, Tannic acid/Fe^{3+} nanoscaffold for interfacial polymerization: Toward enhanced nanofiltration performance. *Environ. Sci. Technol.* **52**, 9341–9349 (2018).
59. Y. Q. Zhang, X. Q. Cheng, X. Jiang, J. U. Jeffrey, C. H. Lau, S. Q. Liu, L. Shao, Robust natural nanocomposites realizing unprecedented ultrafast precise molecular separations. *Mater. Today* **36**, 40–47 (2020).
60. S. N. Ramanan, N. Shahkaramipour, T. Tran, L. Zhu, S. R. Venna, C.-K. Lim, A. Singh, P. N. Prasad, H. Lin, Self-cleaning membranes for water purification by co-deposition of photo-mobile 4,4′-azodianiline and bio-adhesive polydopamine. *J. Membr. Sci.* **554**, 164–174 (2018).
61. Y. Q. Zhang, H. G. Sun, H. Sadam, Y. Liu, L. Shao, Supramolecular chemistry assisted construction of ultra-stable solvent-resistant membranes for angstrom-sized molecular separation. *Chem. Eng. J.* **371**, 535–543 (2019).
62. A. S. Michaels, Analysis and prediction of sieving curves for ultrafiltration membranes: A universal correlation? *Sep. Sci. Technol.* **15**, 1305–1322 (1980).
63. M. Wu, J. Yuan, H. Wu, Y. Su, H. Yang, X. You, R. Zhang, X. He, N. A. Khan, R. Kasher, Z. Jiang, Ultrathin nanofiltration membrane with polydopamine-covalent organic framework interlayer for enhanced permeability and structural stability. *J. Membr. Sci.* **576**, 131–141 (2019).
64. Y. Q. Zhang, J. Ma, L. Shao, Ultra-thin trinity coating enabled by competitive reactions for unparalleled molecular separation. *J. Mater. Chem. A* **8**, 5078–5085 (2020).
65. J. P. Perdew, K. Burke, M. Ernzerhof, Generalized gradient approximation made simple. *Phys. Rev. Lett.* **77**, 3865–3868 (1996).
66. B. Delley, From molecules to solids with the DMol3 approach. *J. Chem. Phys.* **113**, 7756–7764 (2000).
67. B. Delley, An all-electron numerical method for solving the local density functional for polyatomic molecules. *J. Chem. Phys.* **92**, 508–517 (1990).
68. M. Dolg, U. Wedig, H. Stoll, H. Preuss, Energy-adjusted ab initio pseudopotentials for the first row transition elements. *J. Chem. Phys.* **86**, 866–872 (1987).
69. A. Bergner, M. Dolg, W. Küchle, H. Stoll, H. Preuß, Ab initio energy-adjusted pseudopotentials for elements of groups 13–17. *Mol. Phys.* **80**, 1431–1441 (2006).
70. S. Grimme, J. Antony, S. Ehrlich, H. Krieg, A consistent and accurate ab initio parametrization of density functional dispersion correction (DFT-D) for the 94 elements H-Pu. *J. Chem. Phys.* **132**, 154104 (2010).
71. T. A. Halgren, W. N. Lipscomb, The synchronous-transit method for determining reaction pathways and locating molecular transition states. *Chem. Phys. Lett.* **49**, 225–232 (1977).
72. G. Henkelman, H. JoNsson, Improved tangent estimate in the nudged elastic band method for finding minimum energy paths and saddle points. *J. Chem. Phys.* **113**, 9978–9985 (2000).

Acknowledgments: We thank other laboratory members for assistance and the Editage (www.editage.com) for English language editing. **Funding:** This work was supported by the National Natural Science Foundation of China (21878062), the Natural Science Foundation of Heilongjiang Province for Distinguished Young Scholars (JQ2020B001), and the State Key

Laboratory of Urban Water Resource and Environment (Harbin Institute of Technology) (no. 2020DX02). **Author contributions:** L.S. and Y.Z. designed the membrane, performed the experiments, analyzed the results, and wrote the manuscript. All authors participated in the analysis of the experimental results and writing of the manuscript. **Competing interests:** The authors declare that they have no competing interests. **Data and materials availability:** All data needed to evaluate the conclusions in the paper are present in the paper and/or the Supplementary Materials. Additional data related to this paper may be requested from the authors.

Submitted 21 September 2020
Accepted 4 February 2021
Published 24 March 2021
10.1126/sciadv.abe8706

Citation: Y. Zhang, J. Guo, G. Han, Y. Bai, Q. Ge, J. Ma, C. H. Lau, L. Shao, Molecularly soldered covalent organic frameworks for ultrafast precision sieving. *Sci. Adv.* **7**, eabe8706 (2021).

Molecularly soldered covalent organic frameworks for ultrafast precision sieving

Yanqiu Zhang, Jing Guo, Gang Han, Yongping Bai, Qingchun Ge, Jun Ma, Cher Hon Lau and Lu Shao

Sci Adv **7** (13), eabe8706.
DOI: 10.1126/sciadv.abe8706